

Euclid detectability of pair instability supernovae in binary population synthesis models consistent with merging binary black holes

Ataru Tanikawa^{1,*}, Takashi J. Moriya^{2,3,4}, Nozomu Tominaga^{2,3,5,6}, Naoki Yoshida^{7,6,8}

¹Department of Earth Science and Astronomy, College of Arts and Sciences, The University of Tokyo, 3-8-1 Komaba, Meguro-ku, Tokyo 153-8902, Japan

²National Astronomical Observatory of Japan, National Institutes of Natural Sciences, 2-21-1 Osawa, Mitaka, Tokyo 181-8588, Japan

³Department of Astronomical Science, School of Physical Sciences, The Graduate University of Advanced Studies (SOKENDAI), 2-21-1 Osawa, Mitaka, Tokyo 181-8588, Japan

⁴School of Physics and Astronomy, Faculty of Science, Monash University, Clayton, Victoria 3800, Australia

⁵Department of Physics, Faculty of Science and Engineering, Konan University, 8-9-1 Okamoto, Kobe, Hyogo 658-8501, Japan

⁶Kavli Institute for the Physics and Mathematics of the Universe (WPI), The University of Tokyo, 5-1-5 Kashiwanoha, Kashiwa, Chiba 277-8583, Japan

⁷Department of Physics, School of Science, The University of Tokyo, 7-3-1 Hongo, Bunkyo, Tokyo 113-0033, Japan

⁸Research Center for the Early Universe, School of Science, The University of Tokyo, 7-3-1 Hongo, Bunkyo, Tokyo 113-0033, Japan

Accepted XXX. Received YYY; in original form ZZZ

ABSTRACT

We infer the expected detection number of pair instability supernovae (PISNe) during the operation of the *Euclid* space telescope based on binary population models. Our models reproduce the global maximum of the rate at the primary BH mass of $\sim 9 - 10 M_{\odot}$, and the overall gradient of the primary BH mass distribution in the binary BH merger rate consistent with recent observations. We consider different PISN conditions depending on the $^{12}\text{C}(\alpha, \gamma)^{16}\text{O}$ reaction rate. The fiducial and 3σ models adopt the standard and 3σ -smaller reaction rate, respectively. Our fiducial model predicts that *Euclid* detects several hydrogen-poor PISNe. For the 3σ model, detection of ~ 1 hydrogen-poor PISN by *Euclid* is expected if the stellar mass distribution extends to $M_{\text{max}} = 600M_{\odot}$, but the expected number becomes significantly smaller if $M_{\text{max}} = 300M_{\odot}$. We may be able to distinguish the fiducial and 3σ models by the observed PISN rate. This will help us to constrain the origin of binary BHs and the reaction rate, although there remains degeneracy between M_{max} and the reaction rate. PISN ejecta mass estimates from light curves and spectra obtained by follow-up observations would be important to disentangle the degeneracy.

Key words: supernovae: general – black hole mergers – gravitational waves

1 INTRODUCTION

Pair instability supernovae (PISNe) are theoretically predicted as thermonuclear explosions of very massive stars, leaving behind no stellar remnants (e.g. Fowler & Hoyle 1964; Barkat et al. 1967; Fraley 1968; Ober et al. 1983; Bond et al. 1984; El Eid & Langer 1986; Fryer et al. 2001; Heger & Woosley 2002; Umeda & Nomoto 2002; Langer 2012). PISNe have not been conclusively discovered despite of their importance, although there are some possible candidate (e.g., Terreran et al. 2017). Near-solar metallicity stars are hard to keep such massive helium cores until their deaths (Yoshida et al. 2014) unless highly magnetized (Georgy et al. 2017), and only low-metallicity stars are suggested to explode as PISNe (Langer et al. 2007). Since low-metallicity stars are mainly formed at high redshift, near-infrared (NIR) observatories should be appropriate for PISN surveys. Pan et al. (2012), Moriya et al. (2019, 2022b,a), Wong et al. (2019) and Regős et al. (2020) have predicted that PISNe can be discovered by NIR observatories: ULTIMATE-Subaru¹, the Nancy Grace Roman Space Telescope (Spergel et al. 2015), the *Euclid* space telescope

(Laureijs et al. 2011), and the James Webb Space Telescope (Gardner et al. 2006; Whalen et al. 2013).

PISNe can play an important role in shaping black hole (BH) mass distribution in the universe and in binary BHs observed by gravitational wave (GW) observatories (e.g. The LIGO Scientific Collaboration et al. 2021a). They are predicted to form a mass gap in BH mass distribution (Belczynski et al. 2016; Woosley 2017; Spera & Mapelli 2017; Giacobbo et al. 2018; Marchant et al. 2019; van Son et al. 2020; Olejak et al. 2022), hereafter the PI mass gap. The PI mass gap range has been under debate, since it depends on the $^{12}\text{C}(\alpha, \gamma)^{16}\text{O}$ reaction rate (Takahashi 2018; Farmer et al. 2020; Costa et al. 2021; Woosley & Heger 2021; Mehta et al. 2022), stellar metallicity (Farmer et al. 2019; Kinugawa et al. 2021; Farrell et al. 2021; Tanikawa et al. 2021a), stellar wind strength (Belczynski et al. 2020b; Vink et al. 2021), and stellar rotation effect (Glatzel et al. 1985; Mapelli et al. 2020; Marchant & Moriya 2020). The PI mass gap can be buried to some degree if binary BHs are formed through dynamical capture (Rodríguez et al. 2019; Di Carlo et al. 2020; Liu & Bromm 2020; Renzo et al. 2020b; Tagawa et al. 2021; Rizzuto et al. 2021; Costa et al. 2022; Ballone et al. 2022). There are many other suggestions for filling the PI mass gap (Croon et al. 2020; Safarzadeh & Haiman 2020; Ziegler & Freese 2021; Siegel et al.

* E-mail: tanikawa@ea.c.u-tokyo.ac.jp

¹ <https://www.naoj.org/Projects/newdev/ngao/>

2021). Nevertheless, PISNe can have great impacts on binary BH population.

Moriya et al. (2022a) recently investigated the expected numbers of PISN discovery with the *Euclid* space telescope. Their discovery number estimates are based on the PISN event rates that are scaled with the observed event rates of superluminous SNe (Quimby et al. 2013; Prajs et al. 2017). In this paper, we predict the expected PISN detection number by *Euclid*, based on two sets of binary population synthesis models consistent with binary BHs observed by GWs with respect to the global maximum of the rate at the primary BH mass of $\sim 9 - 10 M_{\odot}$, and the global gradient of the primary BH mass distribution in the binary BH merger rate. (Tanikawa et al. 2022). The two models adopt different PISN models in which PISNe happen in stars with helium core mass of $65 - 135$ and $90 - 180 M_{\odot}$. The former and latter models assume the $^{12}\text{C}(\alpha, \gamma)^{16}\text{O}$ reaction rate as the median value of the STARLIB (Sallaska et al. 2013), and one-third of that (or smaller than that by 3σ), respectively. Since PISNe are caused by stars with different masses in the two model series, we obtain different PISN detection numbers. We show that the *Euclid* PISN survey will be helpful to constrain the formation mechanism of binary BHs among a considerable number of suggested scenarios (The LIGO Scientific Collaboration et al. 2021b), and the $^{12}\text{C}(\alpha, \gamma)^{16}\text{O}$ reaction rate. These models do not fully reproduce the details of the primary BH mass distribution in binary BH mergers, such as the second peak of the binary BH merger rate at the primary BH mass of $\sim 35 M_{\odot}$ (The LIGO Scientific Collaboration et al. 2021b). Nevertheless, it is worth while to investigate the models, since they can reproduce the PI mass gap event GW190521 (Abbott et al. 2020a,b), despite considering only the PI mass gap event formed from isolated binary stars.

2 METHOD

We exploit the fiducial and L- 3σ models in Tanikawa et al. (2022). We first explain these previous models. For both models we adopt the models of Madau & Fragos (2017) (MF17) and Skinner & Wise (2020) (SW20) for Population (Pop) I/II and Pop III star formation histories (SFHs), respectively. The average metallicity of Pop I/II evolves in the same way as MF17, and the metallicity is distributed as the log-normal distribution centered on the average metallicity and dispersion of 0.35 at each time. The initial stellar mass functions (IMFs) of single stars and primary stars of binary stars gradually transition from a top-light IMF to a top-heavy IMF with metallicity decreasing, which is motivated by numerical results of Chon et al. (2021). The maximum stellar mass (M_{max}) is $150 M_{\odot}$ for all the metallicities. We perform binary population synthesis simulation by means of BSEEMP² (Tanikawa et al. 2020, 2021a), which is based on the BSE code developed by Hurley et al. (2000, 2002). Different points between the fiducial and L- 3σ models are as follows. The fiducial and L- 3σ models adopt the M and L models, respectively, for single star evolution with metallicity $Z/Z_{\odot} \leq 0.1$ ($Z_{\odot} = 0.02$), while both models adopt the BSE original models for single star evolution with $Z/Z_{\odot} > 0.1$. Their features can be seen in appendix of Tanikawa et al. (2022). In the fiducial and L- 3σ models, PISNe happen for helium core mass of $65 - 135 M_{\odot}$ and $90 - 180 M_{\odot}$, respectively. Note that we also consider pulsational PISNe (PPISNe Heger & Woosley 2002; Woosley et al. 2007; Langer 2012; Chen et al. 2014; Yoshida et al. 2016; Woosley 2017; Marchant et al. 2019;

Table 1. Summary of the previous and current models.

Name	Star	PPISN	PISN	SFH	M_{max}
Previous models					
fiducial	M	45 – 65	65 – 135	MF17+SW20	150
L- 3σ	L	N/A	90 – 180	MF17+SW20	150
Current models					
fid.150	M	45 – 65	65 – 135	H22+SW20	150
fid.300	M	45 – 65	65 – 135	H22+SW20	300
3σ .150	L	N/A	90 – 180	H22+SW20	150
3σ .300	L	N/A	90 – 180	H22+SW20	300
3σ .600	L	N/A	90 – 180	H22+SW20	600

The “star” column indicate adopted single star models for $Z/Z_{\odot} \leq 0.1$. The “PPISN”, and “PISN” columns indicate the mass ranges of helium cores generating PPISNe and PISNe, respectively. The units of the “PPISN”, “PISN” and “ M_{max} ” columns are M_{\odot} . The fiducial and L- 3σ models (previous models) are used in Tanikawa et al. (2022). Other 5 models (current models) are used in this paper. Except for the Pop I/II SFH, the fid.150 and 3σ .150 models are identical to the fiducial and L- 3σ models, respectively.

Farmer et al. 2019; Leung et al. 2019; Renzo et al. 2020a), which occur for helium core mass of $45 - 65 M_{\odot}$, and leave behind $45 M_{\odot}$ BHs in the fiducial model. On the other hand, they do not occur in the L- 3σ model. The different mass ranges are motivated by effects of the $^{12}\text{C}(\alpha, \gamma)^{16}\text{O}$ nuclear reaction rate on star evolution (Takahashi 2018; Farmer et al. 2020).

We modify these models as follows. We choose the model of Harikane et al. (2022) (H22) for Pop I/II SFH instead of the MF17’s model. The H22’s model is based on higher-redshift (z) observations than the MF17’s model, and consistent with the results of Oesch et al. (2018). The star formation rate density of the H22’s model is smaller than the MF17’s model at $z \gtrsim 8$. We prepare initial conditions with larger M_{max} besides the original ones with $M_{\text{max}} = 150 M_{\odot}$ in order to make clear the dependence of PISN detection rates on M_{max} . We summarize the previous and current models in Table 1. The current model series “fid” and “ 3σ ” correspond to the previous fiducial and L- 3σ models, respectively.

We briefly present parameters related to stable mass transfer and common envelope evolution, which play crucial roles for forming binary BHs. We choose these parameters in the same way as in Tanikawa et al. (2022). The stability for stable mass transfer and common envelope evolution is determined by the mass ratio of binary stars depending on whether a donor star has radiative or convective envelope. The mass ratio is given as in BSE. The criteria for a stellar envelope is different between BSE and BSEEMP. Core (shell) helium burning stars have radiative (convective) envelopes in BSE, while stars with $\log T_{\text{eff}}/T \geq 3.65$ (< 3.65) have radiative (convective) envelopes in BSEEMP, where T_{eff} is effective temperature. The formulae of stable mass transfer are the same as in BSE. In stable mass transfer, the maximum fraction of transferred mass is 0.5. We adopt the α formalism for the common envelope evolution (Webbink 1984), and set $\alpha = 1$ and λ of Claeys et al. (2014), where λ is a numerical factor of the binding energy of a stellar envelope, and depends on the envelope structure (de Kool 1990). If a donor star is in the Hertzsprung gap phase, and its mass transfer is unstable, we assume that it merges with its companion star. This is because such a star does not have steep density gradient between its core and envelope (Ivanova & Taam 2004).

Because we focus on PISNe in this Letter, we describe our model relevant to PISNe in more detail. We construct single star evolution

² <https://github.com/atrtnkw/bseemp>

models up to $1280M_{\odot}$, based on simulation results by the HOSHI code (Takahashi et al. 2016, 2018, 2019; Yoshida et al. 2019). The HOSHI code can generate 2 types of single star models referred as the M and L models, which are similar to the GENEC without rotation (Ekström et al. 2012) and Stern (Brott et al. 2011), respectively. Details of generation of the M and L models are described in Appendix A of Tanikawa et al. (2022). Here, we describe the treatment of convective overshoot, which is important for the difference between the M and L models. Actually, the difference between the M and L models is only in the convective overshoot parameter; the parameter for the M model is smaller than for the L model. This makes the maximum radii of stars different in some stellar mass and metallicity ranges. For example, Pop III stars with $90M_{\odot}$ expand to 40 and $3000R_{\odot}$ in the M and L models, respectively. We treat the convective overshoot as a diffusive process above convective regions. The diffusion coefficient of the convective overshoot exponentially decreases with the distance from the convective boundary as

$$D_{\text{cv}}^{\text{ov}} = D_{\text{cv},0} \exp\left(-2 \frac{\Delta r}{f_{\text{ov}} H_{\text{P0}}}\right), \quad (1)$$

(Herwig 2000) where $D_{\text{cv},0}$ and H_{P0} are the diffusion coefficient and the pressure scale height at the convective boundary, respectively, and Δr is the distance from the convective boundary. The overshoot parameter f_{ov} is set to be 0.01 and 0.03 for the M and L models (Yoshida et al. 2019). As seen above, the M model considers inefficient (not without) convective overshoot, because ab initio hydrodynamical simulations show convective boundary mixing (Anders et al. 2022). We stop our single star evolution calculations at the carbon ignition time, although the HOSHI code can follow later star evolution, such as carbon burning and PI mass loss. We assume that supernova mass loss (including PPISN and PISN mass loss) occurs instantaneously at the stopping time. We adopt this modeling in order to match with those in the BSE original models. Single star evolution after the carbon ignition might affect binary star evolution in reality.

We take into account stellar winds modeled by Belczynski et al. (2010) with mass loss of luminous stars (Nieuwenhuijzen & de Jager 1990; Kudritzki et al. 1989), the NJ wind for short. The NJ wind is used when stars are both blue and red supergiants. Under this stellar wind model, a star with $\sim 300M_{\odot}$ and $\sim 0.01Z_{\odot}$ experiences mass loss of $\sim 10^{-3}M_{\odot}\text{yr}^{-1}$ at its red supergiant phase due to the NJ wind. This mass loss rate is similar to the pulsation-driven mass loss (see fig. 5 in Nakauchi et al. 2020). This NJ wind mass loss strips a hydrogen envelope (i.e. about half mass of a zero-age main-sequence star) from a $\geq 100M_{\odot}$ star with $0.1Z_{\odot}$ and a $\geq 200M_{\odot}$ star with $0.01Z_{\odot}$. We adopt the Fryer’s rapid model (Fryer et al. 2012) with PPISN and PISN effects. Note that the Fryer’s rapid model does not form BHs with $\leq 6M_{\odot}$ unlike the Fryer’s delayed model (Fryer et al. 2012) or their latest model (Fryer et al. 2022). The PPISN and PISN effects are similar to those in Belczynski et al. (2016) for the fiducial model, and to those in Belczynski (2020) or “the revised PSN” model in Olejak et al. (2022) for the 3σ model.

We gather PISN events from both single and binary stars. The numbers of single and binary stars are equal, and thus the intrinsic binary fractions in our models are 1, similar to an intrinsic binary fraction $0.69^{+0.09}_{-0.09}$ derived by Sana et al. (2012). We take into account PISNe from close and interacting binary stars, wide and non-interacting binary stars, disrupted binary stars, and binary merger products. Case A mergers yield more massive main-sequence stars than their pre-merger stars, which can form more massive helium cores than their pre-merger stars at their post main-sequence stage. This can increase PISNe (e.g. Vigna-Gómez et al. 2019). On the other hand, case B merger products have the same helium core mass as the pre-merger

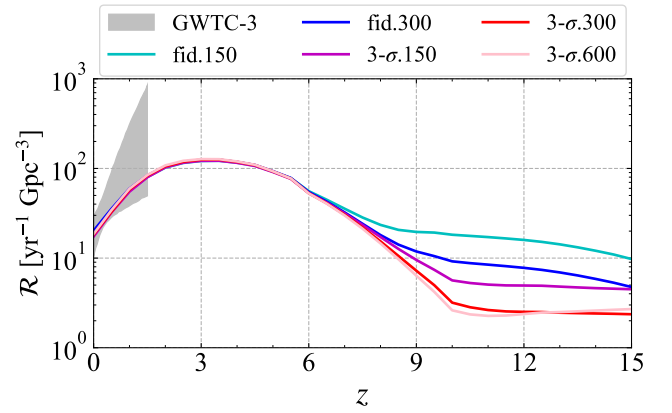


Figure 1. Redshift evolution of binary BH merger rate density (\mathcal{R}) for the current 5 models shown in Table 1. The gray-shaded regions shows the 90 % credible interval inferred by GWTC-3.

stars. They may avoid PISNe if their helium core masses are small (Di Carlo et al. 2020; Renzo et al. 2020b; Costa et al. 2022; Ballone et al. 2022). Mass transfer and mergers rejuvenate the accretors and merger products, respectively, in the same way as in BSE as follows. Regardless of case A and B mass transfers, the age of an accretor is calculated so as to keep the fraction of main-sequence lifetime constant before and after the accretor increases its mass (see the details in section 7.1 of Hurley et al. 2000)³. The age of a case A merger product is determined as eq. (80) of Hurley et al. (2002). The age of a case B merger product is the same as the age of the pre-merger post main-sequence star. These modelings produce the following results in our simulations. Through case A or B mass transfers, a star forms a more massive helium core than a star not undergoing these mass transfers. Similarly, case A merger products form more massive helium cores than the pre-merger stars. This is because of the mass increase, not because of the rejuvenation. Rejuvenation itself is not effective on whether the number of PISNe increases or decreases. In BSE, helium core masses depend only on the terminal-age main-sequence masses, not on stellar evolution histories like rejuvenations⁴. For a case B merger, the merger product is not rejuvenated.

Figures 1 and 2 show the redshift evolution of binary BH merger rate density (\mathcal{R}) and primary BH mass distribution of merging binary BHs at $z = 0$ ($d\mathcal{R}/dm_1$), respectively, for the current 5 models. In all the current models, the redshift evolution and primary BH mass distribution matches well with the 90 % credible interval inferred by the LIGO-Virgo Gravitational-Wave Transient Catalog 3 (GWTC-3), despite that these models are slightly different from the previous models in Tanikawa et al. (2022). Taking a look at the primary BH mass distribution, we can see that the current 5 models reproduce the global maximum at $\sim 9 - 10M_{\odot}$, and the global gradient of the primary BH mass distribution in the binary BH merger rate from $\sim 10M_{\odot}$ to $\sim 100M_{\odot}$. Notably, all the current models form binary BH mergers with $65 - 100M_{\odot}$ BHs, the so-called PI mass gap BHs, like GW190521 (Abbott et al. 2020b,a). Such PI mass BHs are formed from Pop III binary stars in model series “fid” (Tanikawa

³ Hurley et al. (2000) describe how to determine an age of a star decreasing its mass through stellar wind in section 7.1. However, this also applies to how to determine an age of a star increasing its mass through mass transfer.

⁴ In reality, stellar evolution histories can change helium core masses. This is because stellar internal structure can be affected by merger and mass accretion (Hellings 1983, 1984; Renzo & Götzberg 2021).

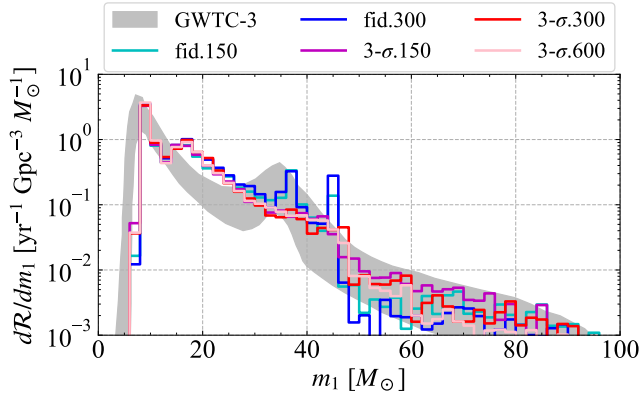


Figure 2. Primary BH mass distribution of merging binary BHs at $z = 0$ (dR/dm_1) for the current 5 models shown in Table 1. The gray-shaded regions shows the 90 % credible interval inferred by GWTC-3.

et al. 2021a), while their origins can be Pop II binary stars in model series “3 σ ” owing to upward shift of the lower mass bound of PISNe (e.g. Belczynski 2020).

We recognize that the current 5 models are not always consistent with the bump at $\sim 35M_\odot$ (see the detail discussions in van Son et al. 2022; Renzo et al. 2022). Although the fiducial models show such bumps, they may disappear depending on the model details. We find that around the bump merging BHs are equally formed through stable mass transfer channel and through common envelope channel due to a small λ parameter of common envelope, despite the fact that merging BHs with $m_1 \gtrsim 20M_\odot$ are mostly formed through stable mass transfer channel (e.g. van Son et al. 2022). This may come from the fact that we calculate stellar mass and radii from our single evolution model, while we obtain convective envelope mass and radii from the original BSE formulae. Nevertheless, even if the bumps are artifacts, the global maximum of the rate at the primary BH mass of $\sim 9 - 10 M_\odot$, and the global gradient of the primary BH mass distribution in the binary BH merger rate are still consistent with GW observations. Moreover, we place high priority on the reproduction of the global structure, especially the PI mass gap BHs. This is because the PI mass gap BHs are directly related to PISNe, the main topic of this paper.

We have performed additional calculations by replacing the fiducial PPISN model with two other PPISN models. The first one is constructed by Renzo et al. (2022) (hereafter Renzo PPISN model), which is based on Farmer et al. (2019). The second one is called “the moderate PPISN model” by Belczynski et al. (2020a), which is based on the hydrodynamics simulations of Leung et al. (2019). PPISNe leave BHs with different masses in the two models, while PPISNe leave only $45 M_\odot$ BHs in the fiducial models. In this sense, the two PPISN models are more realistic than the fiducial models. For Renzo model with $M_{\max} = 150 M_\odot$ and moderate PPISN model with $M_{\max} = 150$ and $300 M_\odot$, the sharp peak at $45 M_\odot$ in Figure 2 is smoothed out. This is a preferable feature from point of view of comparison with the GW observations. On the other hand, for Renzo model with $M_{\max} = 300 M_\odot$, the sharp peak survives, and is shifted to $\sim 55 M_\odot$. Although Renzo model is more realistic than the fiducial model, the primary BH mass distribution deviates from the GW observations. This means that we cannot increase M_{\max} freely for the fiducial models. We have decided to test $M_{\max} = 150$ and $300 M_\odot$ in order to consider a wide range of possibilities, because the primary BH mass distribution in the moderate PPISN model is in good agreement with the GW observations at least.

Our models reproduce merging binary BHs with PI masses even with the fiducial setup. Here, we overview the formation path of such binary BHs. Details of the population synthesis model and related discussions are found in Tanikawa et al. (2021a, 2022). Let us consider Pop III binary stars consisting of $\sim 90M_\odot$ and $\sim 60M_\odot$ stars separated by $\sim 90R_\odot$. The heavier star has a $\sim 40M_\odot$ helium core at its post main-sequence phase, while it expands only to $\sim 40R_\odot$ because of the lack of heavy elements in the atmosphere and of inefficient convective overshoot. The star remains compact and experiences little mass transfer. Note that such a star does not experience common envelope evolution even if it fills its Roche lobe, because it has a radiative envelope and is stable to Roche lobe overflow. With the small-mass helium core surrounded by a massive hydrogen envelope, the star finally collapses to form a $\sim 90M_\odot$ BH without triggering PPISN nor PISN. The lighter (companion) star also evolves through similar processes, and collapses to a $\sim 60M_\odot$ BH. During the binary evolution, the separation does not change significantly because of the absence of mass loss and mass transfer, and thus the two remnant BHs can merge within a Hubble time. It is worth noting that this particular formation process does not occur for binary stars with $\gtrsim 10^{-3}Z_\odot$ (Tanikawa et al. 2022). A $\sim 90M_\odot$ star with $\gtrsim 10^{-3}Z_\odot$ expands to more than $1000R_\odot$ before collapsing to a BH, and loses its hydrogen envelope through mass transfer or common envelope evolution. In our fiducial models, merging binaries of PI mass BHs are not produced for $\gtrsim 10^{-3}Z_\odot$.

From all the current models, we take PISN data including the redshift evolution of PISN rate density, and properties of PISN progenitors, such as masses and stellar types. These information is fed into the *Euclid* survey simulations as conducted by Moriya et al. (2022a). In short, *Euclid* plans to observe their Deep Field (40 deg^2 in total) approximately every half year. Each visit reaches around 25.5 mag in the I_E band and 24.0 mag in the Y_E , J_E , and H_E bands. We refer to Moriya et al. (2022a) and Scaramella et al. (2021) for the details of the *Euclid* observational plan.

By taking the *Euclid* observational plan presented in Moriya et al. (2022a), we use the aforementioned PISN rate densities to estimate the expected number of PISN discoveries in each model. We repeat the survey simulations with the same setup for 10^3 times and report their average discovery numbers. In model series “fid”, once a PISN explode in our survey simulations, we take the PISN light-curve model of the closest mass from Kasen et al. (2011) and estimate its following brightness evolution. In model series “3 σ ”, we do not have corresponding PISN explosion models to estimate their luminosity evolution. For simplicity, we take the closest mass PISN model from Kasen et al. (2011) to estimate the light-curve evolution even in the case of model series “3 σ ”. The PISN mass range of model series “fid” is $65 - 135M_\odot$ while the PISN mass range for model series “3 σ ” is $90 - 180M_\odot$. All PISNe above $135M_\odot$ in model series “3 σ ” are approximated by the $130M_\odot$ PISN model from model series “fid”. We note that some PISNe above $130M_\odot$ may become brighter than $130M_\odot$ to be detected at higher redshifts, but their number density is not high enough to affect our conclusion in this paper.

3 RESULTS

Figure 3 shows the redshift evolution of PISN rate density for the current 5 models. The solid and dashed curves indicate Type I and II PISNe, respectively, where Type I and II PISNe are hydrogen-poor and hydrogen-rich, and have naked helium stars and post main-sequence stars with hydrogen envelopes as their progenitors, respectively. For any models, Type I PISNe become dominant at $z \lesssim 5$. This

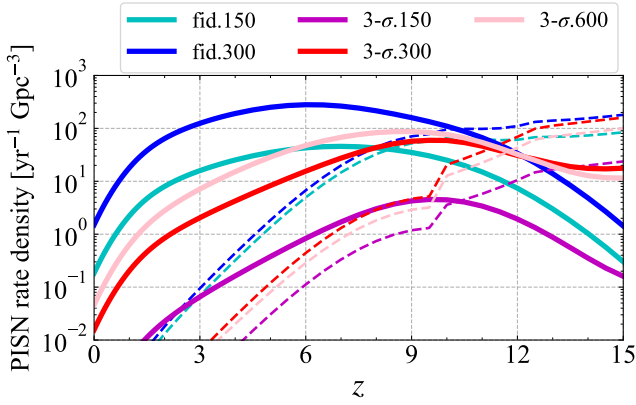


Figure 3. Redshift evolution of PISN rate density for the current 5 models. Solid and dashed curves indicate Type I and II PISNe, respectively, defined in the main text.

is because $\geq 99\%$ of stars have $Z/Z_{\odot} \geq 0.1$ at $z \lesssim 5$, and strip off their hydrogen envelopes due to their stellar winds. The rate densities of Type II PISNe increase with redshift increasing, and exceed those of Type I PISNe at $z \geq 10$. At $z \geq 10$, Pop III stars dominate Type II PISNe. Because of the emergence of Pop III stars, we can see sudden increase of the rate densities of Type II PISNe at $z \sim 10$ for model series “3 σ ”. There is no such increase for model series “fid”. The rate densities of Type II PISNe are high enough to hide the emergence of Pop III stars in model series “fid”. Nevertheless, Pop III stars also dominate Type II PISNe at $z \geq 10$ in model series “fid”.

We compare our PISN rate density with those in [Briel et al. \(2022\)](#). Our fid.300 model roughly corresponds to their “empirical” model, in which they adopt the SFH model of [Madau & Dickinson \(2014\)](#) that is close to our H22 SFH at $z \lesssim 8$. Their M_{\max} is $300M_{\odot}$. Our PISN rate density is about 2 or 3 times smaller than theirs according to their figure 9. We find that this is because our overall metallicity is higher than theirs, and that our adopted stellar evolution model allows massive stars to lose more mass through stronger stellar winds. This argument is consistent with the fact that our binary BH merger rate density is also about 5 times smaller than theirs at $z \lesssim 2$ as seen in their figure 11. If we lowered our metallicity overall, we could obtain larger binary BH merger rate density than shown in Figure 1. However, we remark that our binary BH merger rate density is consistent with that inferred by GWTC-3 with respect to the global maximum of the rate at the primary BH mass of $\sim 9 - 10 M_{\odot}$, and the global gradient of the primary BH mass distribution in the binary BH merger rate.

Hereafter, we focus on Type I PISNe, since *Euclid* will be able to discover PISNe at such low redshifts. We can see in Figure 4 the expected PISN detection numbers within a given z during 6-year *Euclid* operation. In all the cases, the detection numbers saturates beyond $z \sim 3$, despite that the Type I PISN rate densities increase beyond $z \sim 6$. This is because the PISN detection horizon of *Euclid* is $z \sim 3$.

The expected detection numbers in model series “fid” are not sensitive to M_{\max} . In model series “3 σ ”, the detection numbers increase with M_{\max} increasing, but remain smaller than in model series “fid” as can be seen by comparing model 3 σ .600 with fid.150. This is because PISNe in model series “3 σ ” need more massive progenitors than in model series “fid”. In summary, for $M_{\max} = 150 - 300M_{\odot}$, the detection numbers in model series “fid” and “3 σ ” are much more and less than 1, respectively. On the other hand,

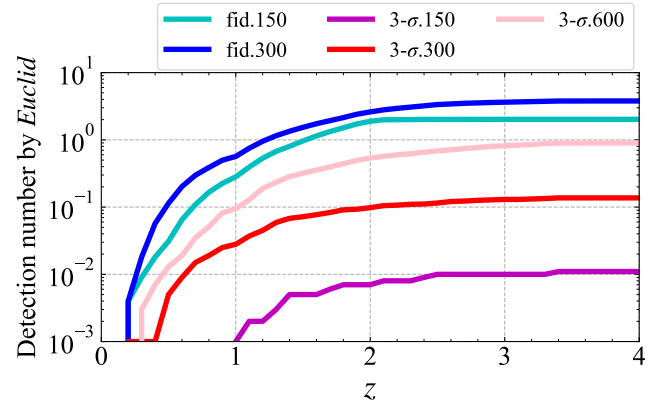


Figure 4. Expected PISN detection numbers to redshift z during 6-year *Euclid* operation.

the detection number can be about 1 in model series “3 σ ” only if $M_{\max} = 600M_{\odot}$.

4 CONCLUSION AND DISCUSSION

We exploit binary population synthesis models consistent with binary BHs observed by GWs with respect to the global maximum of the rate at the primary BH mass of $\sim 9 - 10 M_{\odot}$, and the global gradient of the primary BH mass distribution in the binary BH merger rate to infer the expected PISN detection number by *Euclid*. We find that the expected PISN detection number is greater than 1 in all our “fid” models, but it is significantly smaller in “3 σ ” models under a reasonable assumption of $M_{\max} \lesssim 300M_{\odot}$. Thus, when *Euclid* discovers several or more PISNe, the “fid” model series is clearly preferred, and we can also constrain the $^{12}\text{C}(\alpha, \gamma)^{16}\text{O}$ reaction rate.

If *Euclid* discovers just 1 PISN, it may be difficult to identify the correct model only from the PISN detection number. This is because the expected PISN detection number is close 1 in our model “3 σ ” with $M_{\max} \geq 600M_{\odot}$. We cannot rule out the possibility of $M_{\max} \sim 600M_{\odot}$, although such massive stars have not been discovered. According to the present day mass functions in star clusters R136 and 30 Dor, M_{\max} appears to be at least $\sim 300M_{\odot}$ ([Doran et al. 2013](#); [Schneider et al. 2018a,b](#)). Moreover, the PISN detection numbers of both the “fid” and “3 σ ” models can increase (or decrease) with stellar winds weakening (or strengthening). Unfortunately, there remains substantial uncertainty in the strength of stellar winds (see [Decin 2021](#); [Vink 2022](#), for review). In order to solve this degeneracy, PISN ejecta mass will be helpful. For example, if a future observation discovers a type I PISN with ejecta mass of $180M_{\odot}$, our “3 σ ” model series would be preferred. PISN ejecta mass can be estimated if we can obtain their spectra around the luminosity peak to constrain their expansion velocity, in addition to the light curves obtained by the *Euclid* observations to break the degeneracy between ejecta mass and explosion energy (e.g. [Valenti et al. 2008](#)). Spectroscopic follow-up observations of PISN candidates are essential.

After we can solve the degeneracy, we can also obtain M_{\max} . As seen in Figure 4, the expected PISN detection number depends on M_{\max} . Note that the wind mass loss rate of a massive star is highly uncertain (e.g. [Gräfenr 2021](#); [Vink et al. 2021](#)), and would affect the detection number. The uncertainty would make the measure of M_{\max} difficult, since the detection numbers are similar in the fiducial models with different M_{\max} especially for $z \lesssim 2$.

We make caveats about constraints on the formation mechanism of binary BHs. Even if model series “fid” are correct, it does not always mean that Pop III binary stars form PI mass gap BHs. To be so, Pop III stars have to evolve with inefficient convective overshoot (Tanikawa et al. 2021a,b, 2022). This can be constrained by other PISN surveys as studied in our future work.

ACKNOWLEDGMENTS

We are grateful for the anonymous referee for many helpful suggestions. AT appreciates T. Yoshida and K. Takahashi for many fruitful advices. We thank organizers of the first star and first galaxy conference 2021 in Japan for giving us a good opportunity to start our collaboration. This research could not be accomplished without the support by Grants-in-Aid for Scientific Research (17H06360, 19K03907) from the Japan Society for the Promotion of Science. This work is supported by JSPS Core-to-Core Program (JPJSCCA20210003).

DATA AVAILABILITY

Results will be shared on reasonable request to authors. The results include the additional calculations by the fiducial PPISN model with two other PPISN models: the Renzo’s PPISN and moderate PPISN models, which are discussed in section 2.

REFERENCES

Abbott R., et al., 2020a, *Phys. Rev. Lett.*, **125**, 101102
 Abbott R., et al., 2020b, *ApJ*, **900**, L13
 Anders E. H., Jermyn A. S., Lecoanet D., Brown B. P., 2022, *ApJ*, **926**, 169
 Ballone A., Costa G., Mapelli M., MacLeod M., 2022, arXiv e-prints, p. arXiv:2204.03493
 Barkat Z., Rakavy G., Sack N., 1967, *Phys. Rev. Lett.*, **18**, 379
 Belczynski K., 2020, *ApJ*, **905**, L15
 Belczynski K., Bulik T., Fryer C. L., Ruiter A., Valsecchi F., Vink J. S., Hurley J. R., 2010, *ApJ*, **714**, 1217
 Belczynski K., et al., 2016, *A&A*, **594**, A97
 Belczynski K., et al., 2020a, *A&A*, **636**, A104
 Belczynski K., et al., 2020b, *ApJ*, **890**, 113
 Bond J. R., Arnett W. D., Carr B. J., 1984, *ApJ*, **280**, 825
 Briel M. M., Eldridge J. J., Stanway E. R., Stevance H. F., Chrimes A. A., 2022, *MNRAS*, **514**, 1315
 Brott I., et al., 2011, *A&A*, **530**, A115
 Chen K.-J., Woosley S., Heger A., Almgren A., Whalen D. J., 2014, *ApJ*, **792**, 28
 Chon S., Omukai K., Schneider R., 2021, *MNRAS*, **508**, 4175
 Claeys J. S. W., Pols O. R., Izzard R. G., Vink J., Verbunt F. W. M., 2014, *A&A*, **563**, A83
 Costa G., Bressan A., Mapelli M., Marigo P., Iorio G., Spera M., 2021, *MNRAS*, **501**, 4514
 Costa G., Ballone A., Mapelli M., Bressan A., 2022, *MNRAS*, **516**, 1072
 Croon D., McDermott S. D., Sakstein J., 2020, arXiv e-prints, p. arXiv:2007.07889
 Decin L., 2021, *ARA&A*, **59**, 337
 Di Carlo U. N., Mapelli M., Bouffanais Y., Giacobbo N., Santoliquido F., Bressan A., Spera M., Haardt F., 2020, *MNRAS*, **497**, 1043
 Doran E. I., et al., 2013, *A&A*, **558**, A134
 Ekström S., et al., 2012, *A&A*, **537**, A146
 El Eid M. F., Langer N., 1986, *A&A*, **167**, 274
 Farmer R., Renzo M., de Mink S. E., Marchant P., Justham S., 2019, *ApJ*, **887**, 53

Farmer R., Renzo M., de Mink S. E., Fishbach M., Justham S., 2020, *ApJ*, **902**, L36
 Farrell E., Groh J. H., Hirschi R., Murphy L., Kaiser E., Ekström S., Georgy C., Meynet G., 2021, *MNRAS*, **502**, L40
 Fowler W. A., Hoyle F., 1964, *ApJS*, **9**, 201
 Fraley G. S., 1968, *Ap&SS*, **2**, 96
 Fryer C. L., Woosley S. E., Heger A., 2001, *ApJ*, **550**, 372
 Fryer C. L., Belczynski K., Wiktorowicz G., Dominik M., Kalogera V., Holz D. E., 2012, *ApJ*, **749**, 91
 Fryer C. L., Olejak A., Belczynski K., 2022, *ApJ*, **931**, 94
 Gardner J. P., et al., 2006, *Space Sci. Rev.*, **123**, 485
 Georgy C., Meynet G., Ekström S., Wade G. A., Petit V., Keszthelyi Z., Hirschi R., 2017, *A&A*, **599**, L5
 Giacobbo N., Mapelli M., Spera M., 2018, *MNRAS*, **474**, 2959
 Glatzel W., Fricke K. J., El Eid M. F., 1985, *A&A*, **149**, 413
 Gräfener G., 2021, *A&A*, **647**, A13
 Harikane Y., et al., 2022, *ApJS*, **259**, 20
 Heger A., Woosley S. E., 2002, *ApJ*, **567**, 532
 Hellings P., 1983, *Ap&SS*, **96**, 37
 Hellings P., 1984, *Ap&SS*, **104**, 83
 Herwig F., 2000, *A&A*, **360**, 952
 Hurley J. R., Pols O. R., Tout C. A., 2000, *MNRAS*, **315**, 543
 Hurley J. R., Tout C. A., Pols O. R., 2002, *MNRAS*, **329**, 897
 Ivanova N., Taam R. E., 2004, *ApJ*, **601**, 1058
 Kasen D., Woosley S. E., Heger A., 2011, *ApJ*, **734**, 102
 Kinugawa T., Nakamura T., Nakano H., 2021, *MNRAS*, **501**, L49
 Kudritzki R. P., Pauldrach A., Puls J., Abbott D. C., 1989, *A&A*, **219**, 205
 Langer N., 2012, *ARA&A*, **50**, 107
 Langer N., Norman C. A., de Koter A., Vink J. S., Cantiello M., Yoon S. C., 2007, *A&A*, **475**, L19
 Laureijs R., et al., 2011, arXiv e-prints, p. arXiv:1110.3193
 Leung S.-C., Nomoto K., Blinnikov S., 2019, *ApJ*, **887**, 72
 Liu B., Bromm V., 2020, *ApJ*, **903**, L40
 Madau P., Dickinson M., 2014, *ARA&A*, **52**, 415
 Madau P., Fragos T., 2017, *ApJ*, **840**, 39
 Mapelli M., Spera M., Montanari E., Limongi M., Chieffi A., Giacobbo N., Bressan A., Bouffanais Y., 2020, *ApJ*, **888**, 76
 Marchant P., Moriya T. J., 2020, *A&A*, **640**, L18
 Marchant P., Renzo M., Farmer R., Pappas K. M. W., Taam R. E., de Mink S. E., Kalogera V., 2019, *ApJ*, **882**, 36
 Mehta A. K., Buonanno A., Gair J., Miller M. C., Farag E., deBoer R. J., Wiescher M., Timmes F. X., 2022, *ApJ*, **924**, 39
 Moriya T. J., Wong K. C., Koyama Y., Tanaka M., Oguri M., Hilbert S., Nomoto K., 2019, *PASJ*, **71**, 59
 Moriya T. J., et al., 2022a, *A&A*, **666**, A157
 Moriya T. J., Quimby R. M., Robertson B. E., 2022b, *ApJ*, **925**, 211
 Nakauchi D., Inayoshi K., Omukai K., 2020, *ApJ*, **902**, 81
 Nieuwenhuijzen H., de Jager C., 1990, *A&A*, **231**, 134
 Ober W. W., El Eid M. F., Fricke K. J., 1983, *A&A*, **119**, 61
 Oesch P. A., Bouwens R. J., Illingworth G. D., Labbé I., Stefanon M., 2018, *ApJ*, **855**, 105
 Olejak A., Fryer C. L., Belczynski K., Baibhav V., 2022, *MNRAS*, **516**, 2252
 Pan T., Kasen D., Loeb A., 2012, *MNRAS*, **422**, 2701
 Prajs S., et al., 2017, *MNRAS*, **464**, 3568
 Quimby R. M., Yuan F., Akerlof C., Wheeler J. C., 2013, *MNRAS*, **431**, 912
 Regős E., Vinkó J., Ziegler B. L., 2020, *ApJ*, **894**, 94
 Renzo M., Göteborg Y., 2021, *ApJ*, **923**, 277
 Renzo M., Farmer R., Justham S., Göteborg Y., de Mink S. E., Zapartas E., Marchant P., Smith N., 2020a, *A&A*, **640**, A56
 Renzo M., Cantiello M., Metzger B. D., Jiang Y. F., 2020b, *ApJ*, **904**, L13
 Renzo M., Hendriks D. D., van Son L. A. C., Farmer R., 2022, *Research Notes of the American Astronomical Society*, **6**, 25
 Rizzuto F. P., et al., 2021, *MNRAS*, **501**, 5257
 Rodriguez C. L., Zevin M., Amaro-Seoane P., Chatterjee S., Kremer K., Rasio F. A., Ye C. S., 2019, *Phys. Rev. D*, **100**, 043027
 Safarzadeh M., Haiman Z., 2020, *ApJ*, **903**, L21
 Sallaska A. L., Iliadis C., Champagne A. E., Goriely S., Starrfield S., Timmes F. X., 2013, *ApJS*, **207**, 18

- Sana H., et al., 2012, *Science*, **337**, 444
- Scaramella R., et al., 2021, arXiv e-prints, p. arXiv:2108.01201
- Schneider F. R. N., et al., 2018a, *Science*, **359**, 69
- Schneider F. R. N., et al., 2018b, *A&A*, **618**, A73
- Siegel D. M., Agarwal A., Barnes J., Metzger B. D., Renzo M., Villar V. A., 2021, arXiv e-prints, p. arXiv:2111.03094
- Skinner D., Wise J. H., 2020, *MNRAS*, **492**, 4386
- Spera M., Mapelli M., 2017, *MNRAS*, **470**, 4739
- Spergel D., et al., 2015, arXiv e-prints, p. arXiv:1503.03757
- Tagawa H., Kocsis B., Haiman Z., Bartos I., Omukai K., Samsing J., 2021, *ApJ*, **908**, 194
- Takahashi K., 2018, *ApJ*, **863**, 153
- Takahashi K., Yoshida T., Umeda H., Sumiyoshi K., Yamada S., 2016, *MNRAS*, **456**, 1320
- Takahashi K., Yoshida T., Umeda H., 2018, *ApJ*, **857**, 111
- Takahashi K., Sumiyoshi K., Yamada S., Umeda H., Yoshida T., 2019, *ApJ*, **871**, 153
- Tanikawa A., Kinugawa T., Yoshida T., Hijikawa K., Umeda H., 2021a, *MNRAS*, **505**, 2170
- Tanikawa A., Susa H., Yoshida T., Trani A. A., Kinugawa T., 2021b, *ApJ*, **910**, 30
- Tanikawa A., Yoshida T., Kinugawa T., Takahashi K., Umeda H., 2020, *MNRAS*, **495**, 4170
- Tanikawa A., Yoshida T., Kinugawa T., Trani A. A., Hosokawa T., Susa H., Omukai K., 2022, *ApJ*, **926**, 83
- Terreran G., et al., 2017, *Nature Astronomy*, **1**, 713
- The LIGO Scientific Collaboration et al., 2021a, arXiv e-prints, p. arXiv:2111.03606
- The LIGO Scientific Collaboration The Virgo Collaboration The KAGRA Scientific Collaboration 2021b, arXiv e-prints, p. arXiv:2111.03634
- Umeda H., Nomoto K., 2002, *ApJ*, **565**, 385
- Valenti S., et al., 2008, *MNRAS*, **383**, 1485
- Vigna-Gómez A., Justham S., Mandel I., de Mink S. E., Podsiadlowski P., 2019, *ApJ*, **876**, L29
- Vink J. S., 2022, *ARA&A*, **60**, 203
- Vink J. S., Higgins E. R., Sander A. A. C., Sabhahit G. N., 2021, *MNRAS*, **504**, 146
- Webbink R. F., 1984, *ApJ*, **277**, 355
- Whalen D. J., et al., 2013, *ApJ*, **777**, 110
- Wong K. C., Moriya T. J., Oguri M., Hilbert S., Koyama Y., Nomoto K., 2019, *PASJ*, **71**, 60
- Woosley S. E., 2017, *ApJ*, **836**, 244
- Woosley S. E., Heger A., 2021, *ApJ*, **912**, L31
- Woosley S. E., Blinnikov S., Heger A., 2007, *Nature*, **450**, 390
- Yoshida T., Okita S., Umeda H., 2014, *MNRAS*, **438**, 3119
- Yoshida T., Umeda H., Maeda K., Ishii T., 2016, *MNRAS*, **457**, 351
- Yoshida T., Takiwaki T., Kotake K., Takahashi K., Nakamura K., Umeda H., 2019, *ApJ*, **881**, 16
- Ziegler J., Freese K., 2021, *Phys. Rev. D*, **104**, 043015
- de Kool M., 1990, *ApJ*, **358**, 189
- van Son L. A. C., et al., 2022, *ApJ*, **931**, 17
- van Son L. A. C., et al., 2020, *ApJ*, **897**, 100

This paper has been typeset from a $\text{\TeX}/\text{\LaTeX}$ file prepared by the author.